Efficient Simulation of Doppler-Broadened Rydberg Quantum Receivers via Monte Carlo Wave Functions

Wenjie Ding, Xinyi Y. I. Xu, *Graduate Student Member, IEEE*, Guoda Xie, Xingang Ren, *Senior Member, IEEE*, Yingsong Li, *Senior Member, IEEE*, Wei E. I. Sha, *Fellow, IEEE*, and Zhixiang Huang, *Senior Member, IEEE*

***Abstract*—Theoretical modeling of Rydberg atom-based microwave sensors is often limited by the high computational cost of the density matrix formalism (DMF), especially when resolving transient dynamics in Doppler-broadened vapor cells. We introduce an efficient direct time-domain numerical framework based on the Monte Carlo Wave Function (MCWF) method for Doppler-broadened Rydberg-atom simulations. By incorporating the Doppler effect as a stochastic initialization parameter within individual quantum trajectories, our approach naturally captures thermal broadening, thereby avoiding explicit velocity-grid integration in the MCWF calculation. This reformulates the propagation from a density-matrix representation whose state dimension scales quadratically with the number of levels to a trajectory-based wave-function representation with linear state dimension for each propagated trajectory. We demonstrate that this framework achieves nearly one order of magnitude reduction in runtime under comparable AT-splitting extraction accuracy, while maintaining agreement with the DMF results for the considered observables. The method is further applied to representative time-domain signal-recovery scenarios, including baseband symbol recovery for 8-ary amplitude-shift keying (8-ASK) signals. This work provides a scalable tool for designing and optimizing next-generation Rydberg quantum receivers.**

***Index Terms*—ASK, AT splitting, Doppler broadening, EIT, electromagnetic field measurement, MCWF method, microwave sensing, quantum receivers, Rydberg atoms, thermal vapor cells, transient dynamics.**

I. Introduction

RYDBERG atoms, with their large polarizabilities and strong sensitivity to external fields, have progressed from tools in fundamental quantum optics to an enabling technology for practical microwave sensing applications [1]. By exploiting electromagnetically induced transparency (EIT) and Autler-Townes (AT) splitting, such atomic sensors enable applications ranging from SI-traceable electric field metrology [2], [3], [4], [5], [6], [7], [8], [9], [10], [11], [12], [13], [14], [15], [16] to quantum receivers for amplitude- and phase-modulated communication signals [17], [18], [19], [20], [21], [22], [23], [24], [25], [26], [28], [29]. As the field advances toward complex application scenarios—such as time-domain signal reception, modulation recognition, and vector-field sensing—the demand for rigorous, computationally efficient theoretical and numerical modeling has become critical.

However, accurately simulating Rydberg-atom microwave sensors in thermal vapor cells remains computationally demanding. A widely used approach is the density matrix formalism (DMF) [30], [31], [32], which becomes computationally expensive when modeling realistic thermal vapor cells. In such systems, coherent microwave coupling coexists with dissipative dynamics and significant Doppler-induced inhomogeneous broadening. To predict the thermal-ensemble spectral response within a direct time-domain DMF framework, one must solve the master equation for numerous velocity classes and compute a distribution-weighted average [3]. As the system size increases or the microwave drive becomes time dependent (requiring fine time stepping for transient resolution), the density-matrix representation in a direct time-domain DMF implementation grows quadratically with the number of levels, and the repeated time-marching over many velocity classes can lead to prohibitively long runtimes.

Although steady-state approximations, analytical averaging techniques, Fourier-decomposition methods for nonequilibrium steady states, and open-source Rydberg-sensor simulation tools have been developed to mitigate the computational costs of DMF-based modeling [33], [34], [35], [43], [44], [45], these approaches are often most effective for steady-state, periodic steady-state, or general-purpose density-matrix simulations. Direct time-domain simulation remains useful for studying transient responses and representative signal-recovery processes, because it directly follows the temporal evolution of the atomic response within the finite simulation window rather than relying solely on a steady-state solution. These considerations motivate the development of a computationally efficient direct

Received 9 January 2026; revised 26 May 2026; accepted 23 June 2026. Date of publication 26 June 2026; date of current version 16 July 2026. This work was supported by the National Nature Science Foundation of China under Grant 62371002, Grant 2022YFA1404003, Grant 62571003, Grant U23A20290, Grant U22A2017, Grant 62531001, and Grant 62201003. *(Corresponding author: Guoda Xie.)*

Wenjie Ding, Guoda Xie, Xingang Ren, Yingsong Li, and Zhixiang Huang are with the Key Laboratory of Opto-Electronic Information Acquisition and Manipulation, Hefei 230601, China, also with the Key Laboratory of Intelligent Computing and Signal Processing, Ministry of Education, Anhui University, Hefei 230601, China, also with the Information Materials and Intelligent Sensing Laboratory of Anhui Province, Anhui University, Hefei 230601, China, and also with the Key Laboratory of Electromagnetic Environmental Sensing of Anhui Higher Education Institutes, Anhui University, Hefei 230601, China (e-mail: p24101001@stu.ahu.edu.cn; gdxie@ahu.edu.cn).

Xinyi Y. I. Xu and Wei E. I. Sha are with the Zhejiang Key Laboratory of Intelligent Electromagnetic Control and Advanced Electronic Integration, College of Information Science and Electronic Engineering, Zhejiang University, Hangzhou 310027, China.

Digital Object Identifier 10.1109/JMMCT.2026.3707907

time-domain framework that maintains quantitative accuracy for open-system dynamics in thermal Rydberg atoms.

This paper develops a numerical framework based on the Monte Carlo wave-function (MCWF) method [36], [37], [38], [39], [40], [41], tailored for Rydberg-atom electrometry, to address this challenge. Reformulating the open-system evolution in terms of stochastic quantum trajectories, rather than direct density-matrix propagation, replaces the full density-matrix representation used in the present time-domain DMF baseline with an *M*-component wave-function representation for each propagated trajectory. In this sense, the advantage of MCWF lies in the lower state dimension per propagated sampling object, whereas the overall computational gain still depends on the sampling effort required to achieve a prescribed accuracy. A key novelty of our approach lies in the treatment of thermal motion: instead of performing an explicit integration over velocity classes, we incorporate Doppler shifts by sampling the atomic velocity (and hence the detuning) as a stochastic initialization parameter for each trajectory. In this way, Doppler broadening is captured naturally through statistical sampling, which avoids explicit velocity-class integration in the MCWF calculation.

We demonstrate that this MCWF framework reproduces the DMF results for the observables considered here, including population dynamics, optical coherence, fitted EIT–AT spectra, and extracted AT splittings. Benchmark tests show nearly one order of magnitude shorter runtime at comparable AT-splitting extraction accuracy under the present direct time-domain benchmark. To illustrate practical utility, the framework is applied to simulations of complex dynamic-signal reception, including baseband symbol recovery for 8-ary amplitude-shift keying (8-ASK). Overall, the MCWF framework provides an efficient engine for modeling dynamic Rydberg-atom-based sensors and supports the design of more complex quantum-receiver architectures.

The remainder of this paper is organized as follows. Section II presents the MCWF formulation and numerical implementation for Rydberg-atom-based microwave electrometry, with Doppler broadening incorporated via stochastic velocity sampling. Section III evaluates the method through benchmark comparisons with DMF, including AT-splitting accuracy, time-step selection, sampling-size dependence, and runtime–accuracy trade-offs, and demonstrates performance in time-varying signal scenarios (e.g., AM and 8-ASK). Section IV summarizes the conclusions and discusses potential applications.

II. Method

A. The MCWF Model

First, consider a four-level Rydberg atomic system, as shown in Fig. 1. When the laser frequency resonates with the transition between states $|1\rangle$ and $|2\rangle$, the atoms absorb the incoming light, leading to a reduction in the transmitted intensity. A coupling field resonant between states $|2\rangle$ and $|3\rangle$ then mixes these states into dressed states with shifted energy levels. Due to their opposite phases, destructive interference occurs, resulting in EIT, which enhances the transmitted light intensity. Further application of a microwave field between states $|3\rangle$ and $|4\rangle$ introduces a secondary set of dressed states, splitting the EIT resonance into two peaks.

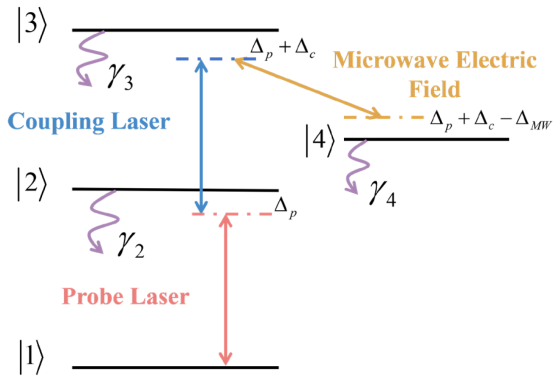

Fig. 1. Four-level Rydberg atomic structure model.

These peaks split according to the microwave Rabi frequency, leading to AT splitting of the EIT signal [28].

Typically, the DMF is used to describe the coherent and dissipative dynamics of a four-level Rydberg system and to generate EIT–AT spectra for electric-field sensing. Its evolution is given by,

$$\dot{\rho}_{4\times4} = -\frac{i}{\hbar}[H_{4\times4}, \rho_{4\times4}] + L(\rho_{4\times4}), \tag{1}$$

where i represents the imaginary unit, $[a, b] = ab - ba$ denotes the commutator, and $H_{4\times4}$ represents the Hamiltonian, and $L(\rho_{4\times4})$ is the Lindblad operator (decoherence matrix). In the direct time-domain implementation considered here, an *M*-level DMF propagates an $M \times M$ density matrix, whose state dimension scales as M^2, and each time step involves matrix operations from the commutator and dissipative terms. When the Doppler effect is considered, averaging over velocity classes is also necessary, which increases both the runtime and memory requirements.

To reduce this matrix–matrix overhead and the resulting memory cost, we adopt the MCWF approach, replacing explicit density matrix propagation with wave function evolution. The wave function then evolves according to the Schrödinger equation,

$$\frac{d\left|\psi^{(n)}(t)\right\rangle}{dt} = -\frac{i}{\hbar}H_{eff}\left|\psi^{(n)}(t)\right\rangle, \tag{2}$$

where H_{eff} denotes the non-Hermitian effective Hamiltonian, and n denotes the n-th trajectory in a system**.** The effective Hamiltonian is defined as,

$$H_{eff} = H_{4\times4} - \frac{i\hbar}{2}\sum_m L_m^\dagger L_m, \tag{3}$$

where $H_{4\times4}$ is the coherent Hamiltonian introduced in (1), and the second non-Hermitian term is constructed from the collapse operators. The coherent Hamiltonian $H_{4\times4}$ is given by,

$$H_{4\times4} = \frac{\hbar}{2}\begin{bmatrix} 0 & \Omega_p & 0 & 0 \\ \Omega_p & -2\Delta_p & \Omega_c & 0 \\ 0 & \Omega_c & -2(\Delta_p+\Delta_c) & \Omega_{MW} \\ 0 & 0 & \Omega_{MW} & -2(\Delta_p+\Delta_c-\Delta_{MW}) \end{bmatrix}. \tag{4}$$

Here Ω_p, Ω_c, and Ω_{MW} represent the Rabi frequencies associated with the probe laser, coupling laser, and microwave electric field, respectively, while Δ_p, Δ_c and Δ_{MW} represent the corresponding frequency detuning for these three externally applied fields. Additionally, $\hbar$ represents the reduced Planck constant.

The second term on the right-hand side of (3) accounts for the dissipative processes in the four-level system, thereby ensuring an equivalent description of the open quantum system as in (1). Specifically, the dissipative dynamics are incorporated through the collapse operators defined as:

$$L_\alpha = \sqrt{\gamma_\alpha}\widehat{C}_\alpha, \tag{5}$$

where α indexes the dissipative channel, $\widehat{C}_\alpha$ denotes the corresponding collapse operator, and γ_α is the associated relaxation or dephasing rate.

To facilitate a rigorous and consistent comparison between the MCWF model and the DMF, a uniform numerical integration scheme based on the second-order Runge–Kutta method is employed throughout this work. The following equations govern the temporal evolution of the wave function:

$$k_1 = -\frac{i}{\hbar}H_{eff}\left|\psi^{(n)}(t)\right\rangle, \tag{6a}$$

$$\left|\psi^{(n)}_{mid}(t)\right\rangle = \left|\psi^{(n)}(t)\right\rangle + \frac{1}{2}dt\cdot k_1, \tag{6b}$$

$$k_2 = -\frac{i}{\hbar}H_{eff}\left|\psi^{(n)}_{mid}(t)\right\rangle, \tag{6c}$$

$$\left|\psi^{(n)}(t+dt)\right\rangle = \left|\psi^{(n)}(t)\right\rangle + dt\cdot k_2, \tag{6d}$$

where k_1 and k_2 are the intermediate slopes of the second-order Runge–Kutta scheme, and $|\psi^{(n)}_{mid}(t)\rangle$ is the intermediate wave function of the n-th trajectory at the midpoint of the time step. These terms describe the deterministic evolution of the wave function over one time step dt, which is then combined with stochastic quantum jumps to capture the dynamics of the open quantum system.

In the MCWF formulation, stochastic quantum jumps are used to model random dissipative processes, with each jump implemented by applying the corresponding collapse operator to the wave function. In the present effective dissipation model, these events include both population-relaxation processes and pure-dephasing processes. As such, accurately capturing the probability of these stochastic events is critical to the fidelity of the simulation.

$$\left\langle\widetilde{\psi}^{(n)}(t+dt)|\widetilde{\psi}^{(n)}(t+dt)\right\rangle = 1 - dp^{(n)}. \tag{7}$$

Substituting (3) and (6) into (7), we get the following expression,

$$dp^{(n)} = \left(\sum_m dp_m^{(n)}\right) = dt\sum_m\left\langle\widetilde{\psi}^{(n)}(t)\right|L_m^\dagger L_m\left|\widetilde{\psi}^{(n)}(t)\right\rangle. \tag{8}$$

Based on the transition probability obtained from (8), the occurrence of a quantum jump at each time step is determined by generating a random number ε uniformly distributed in the interval $[0, 1]$.

If $dp^{(n)} < \varepsilon$, no quantum jump occurs, and the wave function evolves according to the following expression,

$$\left|\psi^{(n)}(t+dt)\right\rangle = \left|\widetilde{\psi}^{(n)}(t+dt)\right\rangle \Big/ \left(1-dp^{(n)}\right)^{1/2}\left(dp^{(n)} < \varepsilon\right). \tag{9}$$

If $dp^{(n)} > \varepsilon$, a quantum jump is deemed to occur. In this case, the probabilities associated with all candidate dissipative channels are evaluated from the corresponding collapse operators and the instantaneous state populations. A weighted random number is then used to select the relevant collapse channel. The updated wave function is subsequently computed as follows,

$$\left|\psi^{(n)}(t+dt)\right\rangle = L_m\left|\widetilde{\psi}^{(n)}(t)\right\rangle \Big/ \left(dp_m^{(n)}\Big/dt\right)^{1/2}\left(dp^{(n)} > \varepsilon\right). \tag{10}$$

Observables and the effective density matrix are reconstructed via ensemble averaging over quantum trajectories. To establish a direct mapping between wave function coefficients and density matrix elements, the wave function for each trajectory is typically expanded in the basis as a superposition,

$$\left|\psi^{(n)}(t)\right\rangle = \sum_m^M c_m^{(n)}\left|m\right\rangle, \tag{11}$$

where $c_m^{(n)}$ is the coefficient of the superposition state. The density matrix elements resulting from trajectory averaging are given by,

$$\rho_{mk} = \frac{1}{N}\sum_n^N c_m^{(n)*}c_k^{(n)}, \tag{12}$$

where N represents the number of trajectories or atoms.

By employing (9) and (10), one can determine the wave functions corresponding to the individual energy levels, from which the density-matrix elements are subsequently computed via (12). Notably, the probe-laser transmission spectrum considered in this work is mainly determined by the coherence term ρ_{21}. In the present direct time-domain DMF baseline, a full $M\times M$ density matrix whereas the MCWF method propagates an M-component wave function for each trajectory. Although not all density-matrix elements are independent in alternative formulations, the density-matrix state representation remains quadratic in M, while the MCWF representation is linear in M for each trajectory.

B. Doppler Effect Involved in the MCWF Model

For moving atoms, the detunings of both the probe and coupling laser frequencies are subject to Doppler shifts. It is important to note that the probe and coupling beams propagate in opposite directions, which determines the respective signs of the Doppler shifts in the following expressions,

$$\widetilde{\Delta}_p^{(n)} = \Delta_p^{(n)} - \frac{2\pi}{\lambda_p}v^{(n)},\ \widetilde{\Delta}_c^{(n)} = \Delta_c^{(n)} + \frac{2\pi}{\lambda_c}v^{(n)}, \tag{13}$$

where v denotes the average velocity of atoms, λ_p and λ_c are the wavelengths of the probe and coupling laser, respectively. Then the Doppler-averaged density matrix element ρ_{21_D} is given by,

$$\rho_{21_D} = \frac{1}{\sqrt{\pi} v_p} \int_{-3v_p}^{3v_p} \rho_{21} \left(\widetilde{\Delta}_p^{(n)}, \widetilde{\Delta}_c^{(n)} \right) e^{\frac{-v^2}{v_p^2}} \mathrm{d}v. \tag{14}$$

where $v_p = \sqrt{2k_B T/m}$, k_B denotes the Boltzmann constant, T is the environmental temperature, and m represents the atomic mass.

Instead of discretizing (14) explicitly, the proposed MCWF framework incorporates Doppler broadening at the trajectory level through stochastic initialization of the atomic velocity. Specifically, each trajectory is initialized by drawing an independent velocity sample v from the Maxwell distribution,

$$f(v) = \frac{1}{\sqrt{\pi} v_p} \exp\left(-\frac{v^2}{{v_p}^2} \right), \tag{15}$$

and the corresponding Doppler-shifted detuning $\Delta_p^{(n)}$ and $\Delta_c^{(n)}$ are then assigned according to (13). The Doppler-broadened density matrix element ρ_{21_D} is finally recovered by ensemble averaging over velocity-resolved quantum trajectories:

$$\rho_{21_D} = \frac{1}{N} \sum_{n}^{N} c_2^{(n)*} \left(\widetilde{\Delta}_p^{(n)}, \widetilde{\Delta}_c^{(n)} \right) \cdot c_1^{(n)} \left(\widetilde{\Delta}_p^{(n)}, \widetilde{\Delta}_c^{(n)} \right). \tag{16}$$

Finally, the transmission power spectrum is evaluated using the following expression,

$$P_{power} = P_{power}^{i} e^{-k_p L C \mathrm{Im}[\rho 21_D]}, \tag{17}$$

where P_{power}^{i} is the incident laser power, $k_p = 2\pi/\lambda_p$ is the wave number of the probe laser L is the propagation distance of the probe laser in the atomic vapor; C is a system parameter defined as $C = -2N_0 \wp_p^2/(\varepsilon_0 \hbar \Omega_p)$, with N_0 being the atomic abundance, $\wp_p$ is the dipole moment for the $|1\rangle$ to $|2\rangle$ transition.

Compared with the present direct time-domain DMF implementation, the proposed MCWF framework incorporates Doppler broadening through trajectory-level velocity sampling, thereby avoiding explicit velocity-grid integration in the MCWF calculation.

III. Numerical Examples and Analysis

A. Validation of MCWF Method Correctness and Benchmark Performance

To verify the correctness and effectiveness of the proposed MCWF method, the atomic levels involved in Fig. 1 correspond to the ^{85}Rb ground state $5S_{1/2}$, the excited state $5P_{3/2}$, and two Rydberg states $52D_{5/2}$ and $53P_{3/2}$. The Rabi frequencies for the probe laser, coupling laser, and microwave electronic field are set as $\Omega_p = 2\pi \times 6$ MHz, $\Omega_c = 2\pi \times 2$ MHz, $\Omega_{MW} = 2\pi \times 1$ MHz, respectively. The time step is set to $dt = 0.01$ ns, and the number of trajectories N is chosen to be 20001. In the dissipation model, population relaxation is described

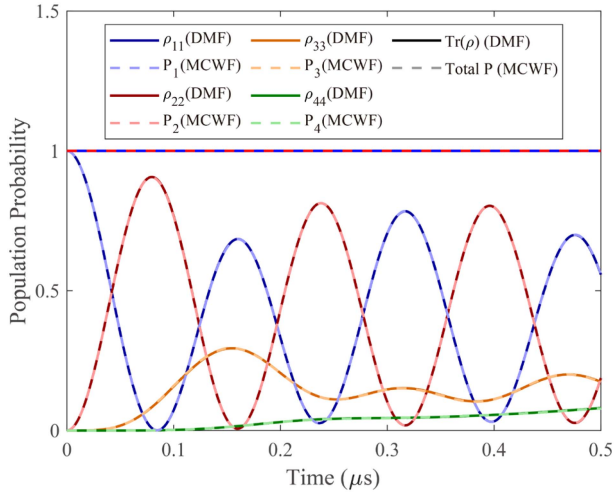

Fig. 2. Temporal evolution of state populations calculated using the DMF and MCWF methods.

by three effective channels, namely $|2\rangle \to |1\rangle$, $|3\rangle \to |2\rangle$, and $|4\rangle \to |1\rangle$, with the corresponding rates $\gamma_2 = 2\pi \times 5$ kHz, $\gamma_3 = 2\pi \times 5$ kHz, and $\gamma_4 = 2\pi \times 40$ kHz, respectively. In addition, to account for environment-induced broadening in warm atomic vapor, a transit-time dephasing rate $\gamma_t = 2\pi \times 0.4$ MHz and a collision-induced dephasing rate $\gamma_{col} = 2\pi \times 0.2$ MHz are introduced as pure-dephasing terms associated with the Rydberg states $|3\rangle$ and $|4\rangle$.

The initial wave function of the system is prepared in the ground state, consistent with the theoretical assumption that, in the absence of external perturbations, the atoms occupy the lowest energy level. Fig. 2 presents the time evolution of the population probabilities computed using the Runge–Kutta method, based on both the MCWF model and the DMF. Specifically, ρ_{11}, ρ_{22}, ρ_{33} and ρ_{44} denote the diagonal density-matrix elements of the DMF, representing the population of each energy level. In contrast, P_1, P_2, P_3, and P_4 correspond to the state populations obtained from the MCWF method, as computed through the stochastic evolution governed by the Schrödinger equation. Additionally, Fig. 2 includes the total population probability for both methods to verify the conservation of probability throughout the temporal evolution ($\sum_{i=1}^{4} \rho_{ii}$ and $\sum_{i=1}^{4} P_i$).

Subsequently, ρ_{21}, which serves as a key parameter for calculating the EIT-AT transmission spectrum, is also calculated and shown in Fig. 3. A high degree of consistency is observed among the results obtained from the MCWF model and those derived from the DMF. Considering that these two approaches are founded on distinct theoretical principles—stochastic wave function evolution versus deterministic density matrix dynamics—such agreement provides compelling validation of the correctness and reliability of the proposed MCWF methodology.

Additionally, the MCWF model is applied to calculate the Doppler-broadened EIT–AT transmission spectrum. The microwave Rabi frequency is set to Ω_{MW}=$2\pi \times 25$ MHz to obtain a clearly resolved AT splitting, while the other Rabi

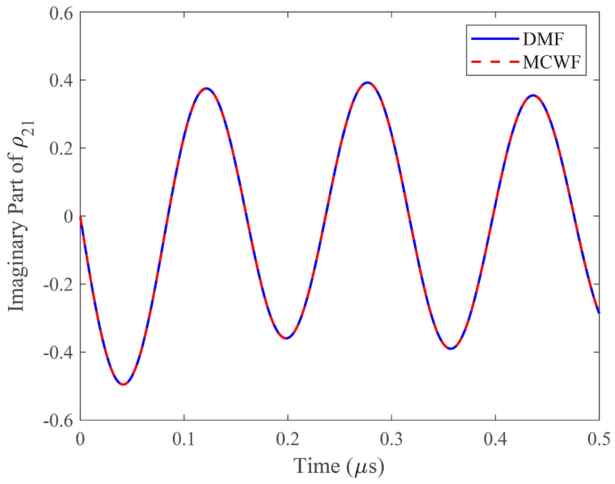

Fig. 3. Temporal evolution of the imaginary part of the coherence term ρ_{21} obtained from the DMF and MCWF methods.

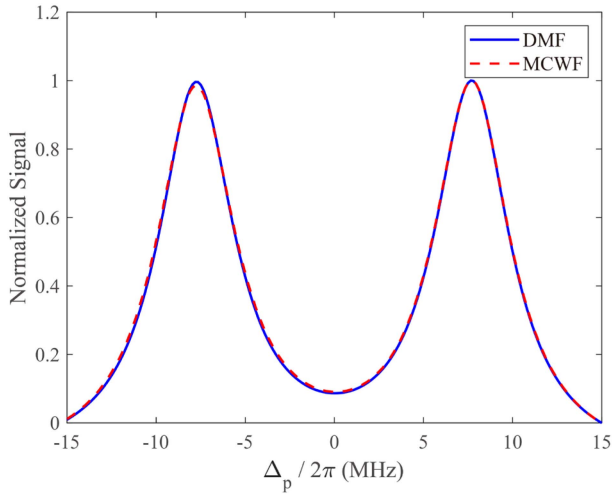

Fig. 4. Normalized comparison of the fitted EIT–AT spectra obtained using the DMF and MCWF methods under identical physical conditions.

frequencies are kept the same as those used in Figs. 2 and 3. The simulations are performed under room-temperature conditions (T = 300 K), and Doppler broadening is incorporated through stochastic velocity sampling in the MCWF approach. The probe detuning is scanned over the range $\Delta_p/2\pi \in [-15, 15]$ MHz with 201 sampling points for both the DMF and MCWF methods, ensuring a consistent spectral resolution for comparison. For the spectrum calculation, the same revised dissipation model is used, while the relaxation rates are set to $\gamma_2 = 2\pi \times 8$ MHz, $\gamma_3 = 2\pi \times 3$ kHz, and $\gamma_4 = 2\pi \times 2$ kHz. The additional warm-vapor dephasing rates are kept as $\gamma_t = 2\pi \times 0.4$ MHz and $\gamma_{col} = 2\pi \times 0.2$ MHz, and are included in the Rydberg-related coherences. Under the same physical parameters, the DMF and MCWF spectra are calculated and then analyzed using the same spectral-extraction procedure, as shown in Fig. 4.

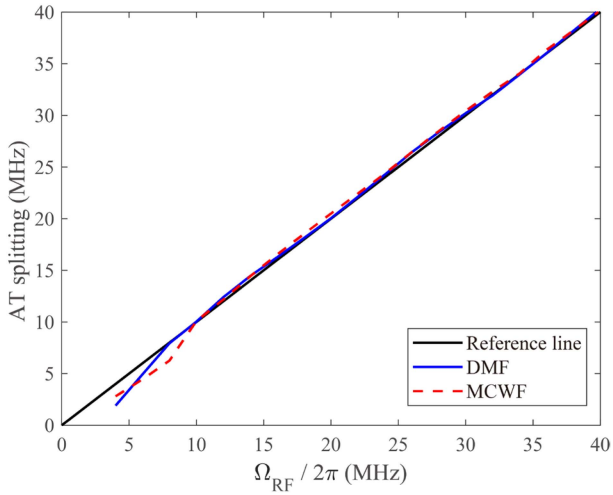

Fig. 5. The AT splitting (Δf_o) versus $\Omega_{MW}/2\pi$.

Fig. 4 presents that the EIT-AT splitting intervals obtained from both simulation approaches exhibit fine agreement, thereby validating the accuracy of the MCWF model. Although discrepancies are present between the MCWF model and the DMF, these differences do not affect the correctness of the final results, as the calculation of the microwave field amplitude depends solely on the EIT-AT splitting intervals.

For a comparative assessment of the accuracy of the numerical results obtained from the MCWF model and the DMF, the amplitude of the microwave electric field was calculated using the following equation [42]:

$$\Omega_{MW}=2\pi\Delta f_{\mathrm{o}} = 2\pi D\Delta f_m,\ |\mathrm{E}_{MW}| = \frac{\hbar}{\wp_{MW}}\Omega_{MW} \quad (18)$$

where $\wp_{MW}$ denotes the transition dipole moment between $|3\rangle$ and $|4\rangle$, and D represents the ratio of the wavelengths of the probe laser to the coupling laser. Here, Δf_m denotes the measured frequency separation between the two EIT–AT peaks in the spectrum, whileΔf_{o} denotes the corresponding AT splitting after the Doppler-mismatch correction. According to (18), $\Omega_{MW} = 2\pi \times 25$ MHz, the analytical amplitude is 1.145 V/m, while the DMF yields 1.151 V/m, and the MCWF model produces a value of 1.152 V/m. These results confirm the suitability of the MCWF model for research on microwave electrometry based on Rydberg atoms.

Furthermore, Fig. 5 shows the linear validation of the extracted AT splitting Δf_o as a function of the microwave Rabi frequency $\Omega_{MW}/2\pi$ obtained using both the MCWF model and the DMF. To maintain consistency with the subsequent benchmark settings, the MCWF results in Fig. 5 are obtained with $N = 20001$ and $dt = 1$ ns, while the DMF results are calculated with $N_v = 401$ and $dt = 0.05$ ns. Here N_v denotes the number of velocity-grid points used to account for Doppler broadening in the density-matrix calculation. All other physical parameters are kept the same as those used for Fig. 4. For consistency, the AT splitting in both the DMF and MCWF results is extracted using the same procedure. The black line denotes the reference

TABLE I
TIME-STEP SELECTION FOR AT-SPLITTING EXTRACTION UNDER FIXED SAMPLING SETTINGS

Methods	Fixed sampling size	*dt* (ns)	Relative error (%)
DMF	401	0.01	1.32
		0.05	1.36
		0.1	92.32
MCWF	20001	0.5	1.24
		1	1.14
		5	95.04

TABLE II
MATCHED-ACCURACY BENCHMARK OF THE DMF AND MCWF METHODS AFTER TIME-STEP SELECTION

Methods	*dt* (ns)	Sampling size	Parallel runtime (s)	Relative error (%)
DMF	0.05	401	1805.71	1.36
MCWF	1	20001	192.78	1.14

relation $\Delta f_o = \Omega_{MW}/2\pi$. The results in Fig. 5 show that the AT splittings extracted from the MCWF spectra agree well with the DMF results and the reference relation, validating the MCWF-based AT-splitting extraction for subsequent microwave electric-field estimation.

Before comparing the computational cost of the two methods, we first verify that the fixed-step second-order Runge–Kutta scheme is sufficient for the present AT-splitting benchmark. The same RK2 scheme is used for both the DMF and MCWF calculations, and the time step for each method is selected according to the convergence of the final extracted AT splitting. Under fixed sampling sizes of $N_v = 401$ for the DMF and $N = 20001$ for the MCWF method, Table I summarizes the dependence of the extracted AT splitting on the time step. For the DMF calculation, increasing the time step from 0.01 ns to 0.05 ns changes the extracted result only slightly, whereas a further increase to 0.1 ns leads to a clear breakdown of the extraction accuracy. For the MCWF method, the extracted AT splitting remains stable when the time step is increased from 0.5 ns to 1 ns, while a much larger step of 5 ns is no longer suitable. Accordingly, the subsequent benchmark adopts $dt = 0.05$ ns for the DMF and $dt = 1$ ns for the MCWF as their representative converged time-step settings.

Using the selected time steps in Table I, Fig. 6 presents the runtime as a function of sampling size. (All runtime measurements reported in Figs. 6 and 7 and Table II were obtained under the same 12-core parallel computing configuration.) For the DMF

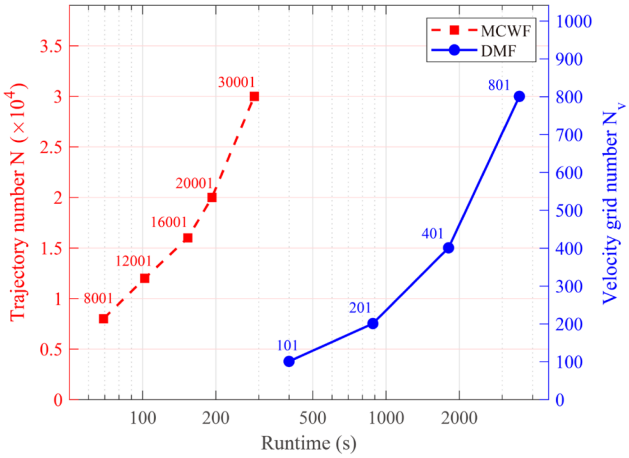

Fig. 6. Runtime versus sampling size using the selected time step for each method.

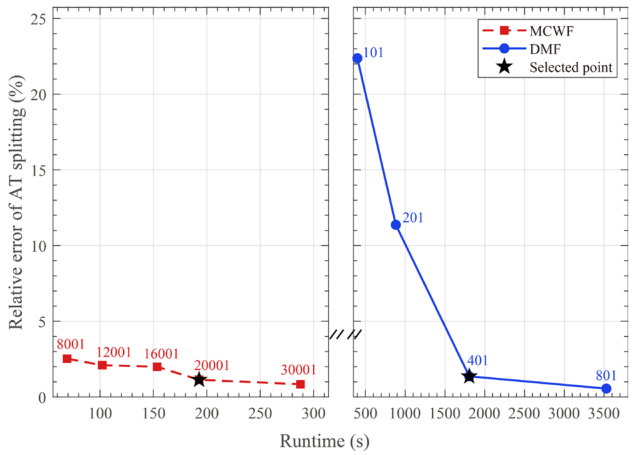

Fig. 7. Runtime–accuracy comparison of the DMF and MCWF methods using the selected time step for each method.

method, the runtime increases monotonically with the number of velocity grid points N_v; for the MCWF method, the runtime likewise increases with the number of trajectories N. Since N_v and N represent different sampling objects—velocity-grid discretization in the DMF and stochastic trajectory sampling in the MCWF—they are shown using separate vertical axes in the same figure, with runtime used as the common horizontal axis. This comparison provides a transparent view of how the computational cost increases with sampling resolution for the two implementations.

To compare the two methods in a common metric space, Fig. 7 further plots the relative error of the extracted AT splitting as a function of runtime. The results show that increasing the sampling size reduces the extraction error for both methods. More importantly, in the low-error regime relevant to the present benchmark, the MCWF method reaches comparable extraction accuracy with a substantially shorter runtime than the DMF implementation. This indicates that, for the present direct time-domain transient benchmark, the MCWF method provides a favorable runtime–accuracy trade-off.

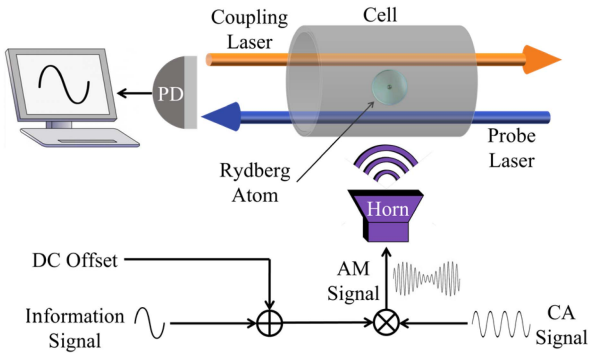

Fig. 8. Atomic reception process based on Rydberg atoms.

Table II gives a representative matched-accuracy comparison based on the results in Fig. 7. With $dt = 0.05$ ns and $N_v = 401$, the DMF calculation yields a relative AT-splitting error of 1.36% with a parallel runtime of 1805.71 s. In comparison, with $dt = 1$ ns and $N = 20001$, the MCWF calculation yields a relative error of 1.14% with a parallel runtime of 192.78 s. Thus, under comparable extraction accuracy, the MCWF implementation requires an approximately 9.36 times shorter runtime than the present direct time-domain DMF baseline.

Under the same physical model, observable definition, AT-splitting extraction procedure, and 12-core parallel computing configuration, the benchmark results in Table II quantify the runtime–accuracy trade-off for the direct time-domain transient simulations considered in this work. This controlled comparison provides a consistent basis for evaluating the computational performance of the two implementations in the present simulation task.

B. Simulation and Application in Microwave Communication Signal Reception

Reference [12] discusses the advantages of the radio receiver system based on Rydberg atoms. Beyond its capability to detect weak signals, the system also enables self-demodulation of the received signals [11]. As illustrated in Fig. 8, an amplitude-modulated (AM) signal is generated by modulating the carrier amplitude (CA), where the carrier frequency is resonant with the atomic energy levels $|3\rangle$ and $|4\rangle$ as shown in Fig. 1, using a baseband signal. This modulated signal is delivered to the atomic vapor cell through a horn antenna. The interaction between the modulated signal and the Rydberg atoms will alter the absorption properties of the system to the probe laser. By analyzing and processing the transmission spectrum of the probe laser detected by a photodetector, the original baseband signal can be retrieved. In this subsection, these reception processes are used as representative time-domain signal-recovery examples to further demonstrate the applicability of the proposed MCWF framework. The atomic and driving-field parameters used in this subsection are kept consistent with those used in the AT-splitting calculation in Section III-A. To focus on the representative time-domain signal-recovery process, the additional transit-time and collision-induced dephasing rates are set to $\gamma_t = \gamma_{col} = 0$ MHz in these simulations.

In the context of numerical simulations for the reception of signals based on Rydberg atoms, two simulation strategies can be adopted. The first strategy involves detecting the amplitude of the transmission spectrum at zero detuning to obtain the baseband signal directly. This method eliminates the need for laser frequency scanning, thereby improving computational efficiency. However, the extracted signal amplitude does not exactly correspond to the original input signal amplitude. The second strategy extracts the signal by measuring the separation between the two peaks in the EIT-AT transmission spectrum. The baseband signal amplitude at any given time can then be determined using (18). Compared to the first approach, this method requires scanning the laser frequency, which reduces computational efficiency. Nevertheless, it enables precise determination of the baseband signal amplitude at each moment.

In the first numerical simulation scheme, the proposed MCWF model is employed to simulate the detection and reception of signals with three distinct waveform types. The corresponding results are shown in Fig. 9(a)–(c), where the black solid line represents the input baseband signal, the blue solid line corresponds to the experimental measurements, and the red dashed line indicates the numerical simulation. The simulated results for the sine, square, and triangular AM signals show good agreement with the experimental data, thereby supporting the applicability of the MCWF model for representative time-domain signal recovery. It is worth noting that the input and received signals in Fig. 9 exhibit a phase inversion. This behavior originates from the zero-detuning detection scheme. Near zero detuning, the detected signal corresponds to the probe transmission around the center of the EIT resonance. As the microwave field increases, the EIT resonance undergoes stronger AT splitting, and the spectral weight shifts from the center toward the two side peaks. Consequently, the transmission amplitude at the zero-detuning point decreases as the microwave-field amplitude increases, leading to an approximately inverted received waveform.

Additionally, the MCWF model is employed to simulate the reception of a 30-bit 8-ary amplitude-shift keying (8ASK) signal using the second simulation strategy. The results are presented in Fig. 10, where the input signal is shown alongside the received signal obtained from the MCWF simulation. As illustrated, the received waveform closely matches the input, demonstrating that the MCWF framework can recover the baseband symbol sequence in this representative time-domain task. These results further confirm its effectiveness as a reliable numerical simulation tool for modeling microwave electric field detection and reception based on Rydberg atom systems.

C. Numerical Verification of MCWF Convergence in Multi-Level Models

To examine whether the convergence requirement of the MCWF method varies with the number of energy levels M the same physical parameters and numerical settings as those used in Figs. 2 and 3 are adopted. Equivalent models with $M = 2, 3, 4$ are constructed by setting the couplings and decay parameters associated with higher levels to zero, thereby ensuring that

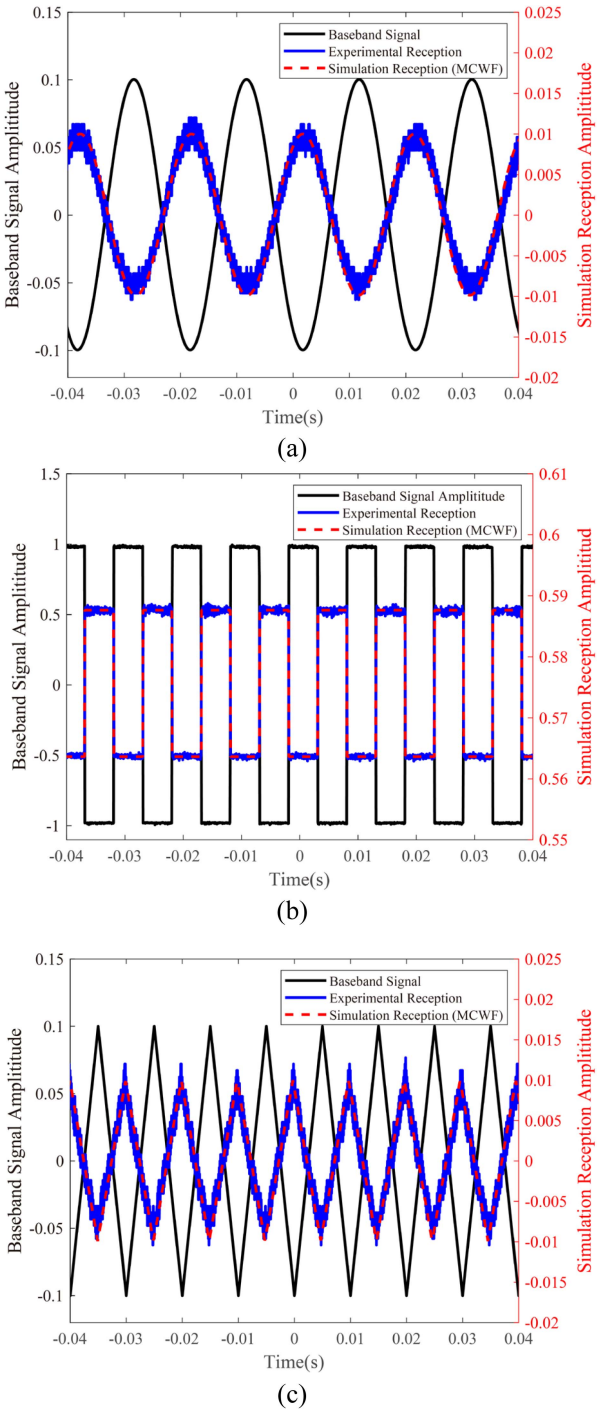

Fig. 9. Reception of AM signals in a Rydberg atom-based receiver system. (a) Sine wave AM signal (50 Hz), (b) Square wave AM signal (100 Hz), (c) Triangular wave AM signal (100 Hz).

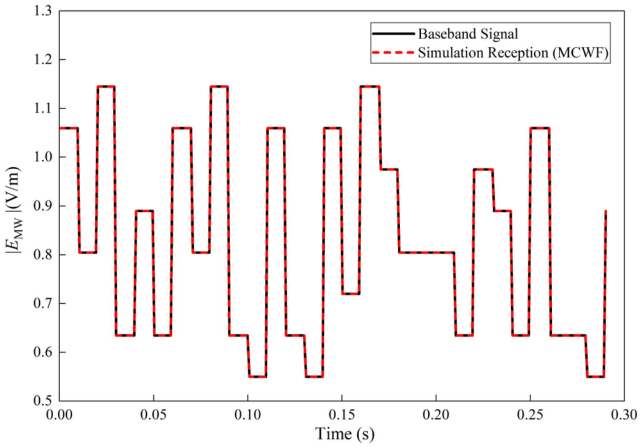

Fig. 10. Results of Rydberg atoms receiving a 30-bit 8ASK signal.

TABLE III
RELATIVE ERROR (%) OF MCWF FOR DIFFERENT ENERGY LEVEL NUMBERS M AND TRAJECTORY NUMBERS N

N	$M=2$	$M=3$	$M=4$
8001	0.69	0.51	0.73
16001	0.41	0.28	0.19
20001	0.18	0.12	0.10

results obtained for different M are directly comparable within a unified framework.

Under the zero-detuning condition $\Delta_p = 0$, the density matrix reconstructed from MCWF trajectories is comparison with the DMF reference solution. Over the same evolution time $T = 50$ ns the numerical integration result of the DMF method for the master equation is taken as the reference solution. Using identical physical parameters and time-sampling points, the number of trajectories N in MCWF is then swept, and the agreement between MCWF and DMF is quantified by the relative error err in percentage.

$$err = \left[\frac{\left\| \rho^{\mathrm{MCWF}} - \rho^{\mathrm{DMF}} \right\|_2}{\left\| \rho^{\mathrm{DMF}} \right\|_2} \right]^{1/2} \times 100 \tag{19}$$

Table III reports the resulting errors for $M = 2, 3, 4$ at different values of N. As N increases, the error exhibits an overall decreasing trend. At the representative trajectory number $N = 20001$ used in this work, the errors for $M = 2, 3, 4$ are all small and remain at a comparable level. Therefore, under the parameter regime and error metric considered here, the MCWF reconstruction shows consistent agreement with the DMF reference solution for the tested energy-level numbers. This indicates that, within the tested range, the trajectory number required to reach a fixed accuracy does not show a pronounced dependence on M, suggesting that the MCWF sampling requirement is approximately independent of the number of levels.

IV. CONCLUSION

Efficient transient simulation of Doppler-broadened thermal-vapor Rydberg microwave sensors is important for system-level design and parameter optimization, yet DMF solvers often become computationally expensive when velocity-resolved averaging and fine time stepping are required. This paper presents an MCWF-based trajectory framework, where open-system dynamics are modeled through stochastic quantum trajectories rather than the full ensemble density matrix. By replacing density-matrix propagation with a trajectory-based wave-function representation, the proposed framework reduces

the state dimension of each propagated sampling object from quadratic to linear scaling with the number of levels. Meanwhile, Doppler broadening is incorporated through Maxwell-distributed velocity sampling at trajectory initialization, avoiding explicit velocity-grid integration in the MCWF calculation while retaining the underlying thermal-ensemble physics.

Benchmark studies indicate that the proposed MCWF approach agrees with DMF for the considered observables, including population dynamics, optical coherence, fitted EIT–AT spectra, and extracted AT splittings. After time-step selection, the MCWF implementation achieves comparable AT-splitting extraction accuracy with an approximately 9.36 times shorter runtime than the present direct time-domain DMF baseline. These results demonstrate the computational benefit of the MCWF framework for the direct time-domain transient simulation considered in this work. The framework is further applied to representative time-domain signal-recovery scenarios, including reception and baseband symbol recovery of 8-ASK signals.

Overall, the MCWF framework provides a computationally scalable simulation tool for dynamic Rydberg-atom-based microwave sensing and quantum reception, facilitating faster parameter sweeps and design exploration. Future work may include adaptive strategies for trajectory sampling and time stepping, extensions to more complex multilevel schemes and vector-field sensing configurations, and systematic validation against experimental measurements across broader operating conditions.

REFERENCES

[1] N. Šibalic and C. S. Adams, *Rydberg Physics*. Bristol, U.K.: IOP, 2018, pp. 2399–2891.

[2] D. A. Anderson, R. E. Sapiro, and G. Raithel, "A self-calibrated SI-traceable Rydberg atom-based radio frequency electric field probe and measurement instrument," *IEEE Trans. Antennas Propag.*, vol. 69, no. 9, pp. 5931–5941, Sep. 2021.

[3] C. L. Holloway et al., "Electric field metrology for SI traceability: Systematic measurement uncertainties in electromagnetically induced transparency in atomic vapor," *J. Appl. Phys.*, vol. 121, no. 23, Jun. 2017, Art. no. 234903.

[4] J. A. Sedlacek et al., "Microwave electrometry with Rydberg atoms in a vapour cell using bright atomic resonances," *Nature Phys.*, vol. 8, no. 11, pp. 819–824, Sep. 2012.

[5] S. E. Harris, "Electromagnetically induced transparency," *Phys. Today*, vol. 50, no. 7, pp. 36–42, Jul. 1997.

[6] M. D. Lukin et al., "Quantum interference effects induced by interacting dark resonances," *Phys. Rev. A*, vol. 60, no. 4, pp. 3225–3228, Oct. 1999.

[7] M. Fleischhauer, A. Imamoglu, and J. P. Marangos, "Electromagnetically induced transparency: Optics in coherent media," *Rev. Mod. Phys.*, vol. 77, no. 2, pp. 633–673, Apr. 2005.

[8] J. A. Sedlacek et al., "Atom-based vector microwave electrometry using rubidium Rydberg atoms in a vapor cell," *Phys. Rev. Lett.*, vol. 111, no. 6, Aug. 2013, Art. no. 063001.

[9] M. T. Simons et al., "Using frequency detuning to improve the sensitivity of electric field measurements via electromagnetically induced transparency and Autler-Townes splitting in Rydberg atoms," *Appl. Phys. Lett.*, vol. 108, no. 17, Apr. 2016, Art. no. 174101.

[10] J. A. Gordon et al., "Weak electric-field detection with sub-1 Hz resolution at radio frequencies using a Rydberg atom-based mixer," *AIP Adv.*, vol. 9, no. 4, Apr. 2019, Art. no. 045030.

[11] M. Jing et al., "Atomic superheterodyne receiver based on microwave-dressed Rydberg spectroscopy," *Nature Phys.*, vol. 16, no. 9, pp. 911–915, Sep. 2020.

[12] M. T. Simons et al., "A Rydberg atom-based mixer: Measuring the phase of a radio frequency wave," *Appl. Phys. Lett.*, vol. 114, no. 11, Mar. 2019, Art. no. 114101.

[13] M. Cai et al., "Sensitivity improvement and determination of Rydberg atom-based microwave sensor," *Photonics*, vol. 9, no. 4, Apr. 2022, Art. no. 250.

[14] Y. Peng et al., "Cavity-enhanced microwave electric field measurement using Rydberg atoms," *J. Opt. Soc. Amer. B*, vol. 35, no. 9, pp. 2272–2277, Sep. 2018.

[15] A. Zhou et al., "High-sensitivity Rydberg atom-based field sensing enhancement using miniaturized resonator," *IEEE Trans. Antennas Propag.*, vol. 73, no. 12, pp. 10948–10952, Dec. 2025, doi: 10.1109/TAP.2025.3596373.

[16] C. L. Holloway et al., "Broadband Rydberg atom-based electric-field probe for SI-traceable, self-calibrated measurements," *IEEE Trans. Antennas Propag.*, vol. 62, no. 12, pp. 6169–6182, Dec. 2014.

[17] Z. Song et al., "Rydberg-atom-based digital communication using a continuously tunable radio-frequency carrier," *Opt. Exp.*, vol. 27, no. 6, pp. 8848–8857, Mar. 2019.

[18] C. L. Holloway et al., "Detecting and receiving phase-modulated signals with a Rydberg atom-based receiver," *IEEE Antennas Wireless Propag. Lett.*, vol. 18, no. 9, pp. 1853–1857, Sep. 2019.

[19] Y. Jiao et al., "Atom-based receiver for amplitude-modulated baseband signals in high-frequency radio communication," *Appl. Phys. Exp.*, vol. 12, no. 12, Dec. 2019, Art. no. 126002.

[20] J. A. Gordon et al., "Millimeter wave detection via Autler-Townes splitting in rubidium Rydberg atoms," *Appl. Phys. Lett.*, vol. 105, no. 2, Jul. 2014, Art. no. 024104.

[21] M. T. Simons et al., "Electromagnetically induced transparency (EIT) and Autler-Townes (AT) splitting in the presence of band-limited white Gaussian noise," *J. Appl. Phys.*, vol. 123, no. 20, May 2018, Art. no. 203101.

[22] D. H. Meyer et al., "Digital communication with Rydberg atoms and amplitude-modulated microwave fields," *Appl. Phys. Lett.*, vol. 112, no. 21, May 2018, Art. no. 211108.

[23] D. A. Anderson, R. E. Sapiro, and G. Raithel, "An atomic receiver for AM and FM radio communication," *IEEE Trans. Antennas Propag.*, vol. 69, no. 5, pp. 2455–2462, May 2021.

[24] M. G. Bason et al., "Enhanced electric field sensitivity of rf-dressed Rydberg dark states," *New J. Phys.*, vol. 12, no. 6, Jun. 2010, Art. no. 065015.

[25] H. Zou et al., "Atomic receiver by utilizing multiple radio-frequency coupling at Rydberg states of rubidium," *Appl. Sci.*, vol. 10, no. 4, Feb. 2020, Art. no. 1346.

[26] C. G. Wade et al., "Real-time near-field terahertz imaging with atomic optical fluorescence," *Nature Photon.*, vol. 11, no. 1, pp. 40–43, Jan. 2017.

[27] Y. Jiao et al., "Atom-based receiver for amplitude-modulated baseband signals in high-frequency radio communication," *Appl. Phys. Exp.*, vol. 12, no. 12, Dec. 2019, Art. no. 126002.

[28] Z. K. Liu et al., "Deep learning enhanced Rydberg multifrequency microwave recognition," *Nature Commun.*, vol. 13, no. 1, Apr. 2022, Art. no. 1997.

[29] C. L. Holloway et al., "Sub-wavelength imaging and field mapping via electromagnetically induced transparency and Autler-Townes splitting in Rydberg atoms," *Appl. Phys. Lett.*, vol. 104, no. 24, Jun. 2014, Art. no. 244102.

[30] Y. Yang and Y. Fang, "Modified two-derivative Runge–Kutta methods for the schrödinger equation," *J. Math. Chem.*, vol. 56, no. 3, pp. 799–812, Mar. 2018.

[31] L. Hernández-Sánchez et al., "Numerical solution of the Lindblad master equation using the Runge-Kutta method implemented in Python," *Rev. Mex. Fis. E*, vol. 23, no. 1, Jun. 2026, Art. no. 010214, doi: 10.31349/RevMexFisE.23.010214.

[32] D. Manzano, "A short introduction to the Lindblad master equation," *AIP Adv.*, vol. 10, no. 2, Feb. 2020, Art. no. 025106.

[33] S. W. Su et al., "Dynamics of slow light and light storage in a Doppler-broadened electromagnetically-induced-transparency medium: A numerical approach," *Phys. Rev. A*, vol. 83, no. 1, Jan. 2011, Art. no. 013827.

[34] J. H. Wu, M. Artoni, and G. C. La Rocca, "Stationary light pulses in cold thermal atomic clouds," *Phys. Rev. A*, vol. 82, no. 1, Jul. 2010, Art. no. 013807.

[35] X. Y. I. Xu et al., "Fast simulation for interacting four-level Rydberg atoms: Electromagnetically induced transparency and Autler-Townes splitting," *Opt. Exp.*, vol. 32, no. 12, pp. 21755–21766, Jun. 2024.

[36] K. Mølmer, Y. Castin, and J. Dalibard, "Monte Carlo wave-function method in quantum optics," *J. Opt. Soc. Amer. B*, vol. 10, no. 3, pp. 524–538, Mar. 1993.

[37] R. Dum, P. Zoller, and H. Ritsch, "Monte Carlo simulation of the atomic master equation for spontaneous emission," *Phys. Rev. A*, vol. 45, no. 7, pp. 4879–4887, Apr. 1992.

[38] K. Mølmer and Y. Castin, "Monte Carlo wavefunctions in quantum optics," *Quantum Semiclassical Opt.*, vol. 8, no. 1, pp. 49–72, Feb. 1996.
[39] H. Carmichael, *An Open Systems Approach to Quantum Optics*. Berlin, Germany: Springer, 2009.
[40] C. W. Gardiner, "Wave-function quantum stochastic differential equations and quantum-jump simulation methods," *Phys. Rev. A*, vol. 46, no. 7, pp. 4363–4374, Oct. 1992.
[41] P. Zoller, M. Marte, and D. F. Walls, "Quantum jumps in atomic systems," *Phys. Rev. A*, vol. 35, no. 1, pp. 198–207, Jan. 1987.
[42] B. Liu et al., "Electric field measurement and application based on Rydberg atoms," *Electromagn. Sci.*, vol. 1, no. 2, pp. 1–16, Jun. 2023.
[43] O. Nagib and T. G. Walker, "Exact steady state of perturbed open quantum systems," *Phys. Rev. Res.*, vol. 7, no. 3, Jul. 2025, Art. no. 033076.
[44] B. Kasza et al., "Atomic-optical interferometry in fractured loops: A general solution for Rydberg radio-frequency receivers," *Phys. Rev. A*, vol. 111, no. 5, May 2025, Art. no. 053718.
[45] B. N. Miller et al., "RydIQule: A graph-based paradigm for modeling Rydberg and atomic sensors," *Comput. Phys. Commun.*, vol. 294, Jan. 2024, Art. no. 108952.

Wenjie Ding is currently working toward the Ph.D. degree in electronic science and technology with Anhui University, Hefei, China. Her research interests include Rydberg-atom-based quantum sensing, quantum receivers, microwave electric-field measurement, open quantum systems, computational electromagnetics, and numerical methods for light–matter interactions.

Xinyi Y. I. Xu (Graduate Student Member, IEEE) received the B.Eng. degree from Xidian University, Xi'an, China. He is currently working toward the Ph.D. degree with Zhejiang University, Hangzhou, China. His research interests include multiphysics modeling of Rydberg atoms, Rydberg-atom-based sensing and communication applications, including direction-of-arrival estimation, imaging, communications, and MIMO systems, phase retrieval, and electromagnetic inverse scattering problems.

Guoda Xie was born in Anhui, China, in 1991. He received the M.S. and Ph.D. degrees from the School of Electronics and Information Engineering, Anhui University, Hefei, China, in 2017 and 2020, respectively. His research interests include computational electromagnetics (CEM), unconditionally stable finite difference time domain algorithm, multigrid and multiphysics modeling with time domain numerical methods, and antennas.

Xingang Ren (Senior Member, IEEE) received the Ph.D. degree from the Department of Electrical and Electronic Engineering, The University of Hong Kong, Hong Kong, in 2016. He is currently a Full Professor with the State Key Laboratory of Opto-Electronic Information Acquisition and Protection Technology, Anhui University, Hefei, China. He has authored or coauthored more than 90 peer-reviewed journal articles. His research interests include computational electromagnetics (CEM), multiphysics and interdisciplinary studies, plasmonics, emerging optoelectronics (photovoltaics and light emitting diodes), and metasurfaces. In 2022, Prof. Ren was awarded the Second Prize of Science and Technology by the Anhui Provincial Government, China.

Yingsong Li (Senior Member, IEEE) received the B.S. degree in electrical and information engineering and the M.S. degree in electromagnetic field and microwave technology from Harbin Engineering University, Harbin, China, in 2006 and 2011, respectively, the Ph.D. degree in electromagnetic field and microwave technology from the Kochi University of Technology (KUT), Kochi, Japan, and the second Ph.D. degree from Harbin Engineering University, in 2014.

From 2014 to 2022, he was a Full Professor with Harbin Engineering University, Visiting Scholar with the University of California, Davis, CA, USA, from 2016 to 2017, Visiting Professor with the University of York, York, U.K., in 2018, and Visiting Professor with Far Eastern Federal University and KUT. From 2016 to 2021, he was a Postdoc with the Key Laboratory of Microwave Remote Sensing. Chinese Academy of Sciences. Since 2018, he has been the Visiting Professor position with the School of Information, KUT. Since 2022, he has been a Full Professor with the School of Electronic and Information Engineering. Anhui University, Hefei, China. He has authored or coauthored more than 300 journal and conference papers in various areas of electrical and information engineering. His current research interests include signal processing, adaptive filters, metasurface designs, and microwave antennas.

Dr. Li is a fellow of Applied Computational Electromagnetics Society and also a senior member of the Chinese Institute of Electronics.

Wei E. I. Sha (Fellow, IEEE) received the Ph.D. degree in electromagnetic fields and microwave technology from Anhui University, Hefei, China, in 2008. From 2008 to 2017, he was a Postdoctoral Research Fellow and a Research Assistant Professor with the Department of Electrical and Electronic Engineering, the University of Hong Kong. He held a Marie Skłodowska-Curie Individual Fellowship with University College London, London, U.K., from 2018 to 2019. He is currently a Tenured Associate Professor with the College of Information Science and Electronic Engineering, Zhejiang University, Hangzhou, China.

His research interests include theoretical and applied electromagnetics, with a focus on computational electromagnetics, quantum electromagnetics, and electromagnetic information. He has authored or coauthored two books, ten book chapters, more than 220 peer-reviewed journal articles, and 200 conference papers. His works have been cited more than 13164 times on Google Scholar, resulting in an h-index of 60.

He was an Associate Editor for the IEEE JOURNAL ON MULTISCALE AND MULTIPHYSICS COMPUTATIONAL TECHNIQUES, IEEE OPEN JOURNAL OF ANTENNAS AND PROPAGATION, and *Electromagnetic Science*. Dr. Sha is a National Distinguished Young Scholar and a recipient of the 2022 ACES Technical Achievement Award, the Second Prize of Science and Technology Award of the China Institute of Communications, the Second Prize for Science and Technology from the Anhui Provincial Government, and 11 international conference paper awards.

Zhixiang Huang (Senior Member, IEEE) was born in Anhui, China, in 1979. He received the B.S. and Ph.D. degrees from Anhui University (AHU), Hefei, China, in 2002 and 2007, respectively. Since 2008, he has been a Full Professor with the School of Electronic Information and Engineering, AHU. From 2010 to 2011, he was a Visiting Scholar with Iowa State University, Ames, IA, USA. From August 2013 to October 2013, he was a Visiting Professor with The University of Hong Kong, Hong Kong. From 2014 to 2015, he was a Visiting Professor with the Beijing National Laboratory for Condensed Matter Physics, Institute of Physics, Chinese Academy of Sciences, Beijing, China. He has coauthored one monograph on the symplectic finite-difference time-domain method and two book chapters for CRC Press and In Tech Publishers. He has coauthored 90 peer-reviewed journal articles included in the Web of Science Core Collection. His current research interests include time-domain numerical methods, metamaterials, and active antennas.

Dr. Huang was the recipient of the Second Prize of Science and Technology from Anhui Province Government, China, in 2015, and the National Science Foundation for Outstanding Young Scholar of China, in 2017.